EDGE ARTICLE

Check for updates

All publication charges for this article have been paid for by the Royal Society of Chemistry

Accelerated active phase transformation of NiO powered by Pt single atoms for enhanced oxygen evolution reaction†

Chao Lin,‡[a] Yonghui Zhao,[a] Haojie Zhang,[a] Songhai Xie,[b] Ye-Fei Li,*[b] Xiaopeng Li, [iD] *[a] Zheng Jiang*[c] and Zhi-Pan Liu [iD] [b]

Phase transformation of electrode materials widely occurs in electrocatalytic reactions. Metal oxides are promising electrocatalysts for the oxygen evolution reaction (OER); their phase transformation is a key step for the multi-electron OER, and requires extra overpotential. However, little attention has been paid to accelerating and enhancing the phase transformation. Here, we report for the first time that single-atom Pt incorporated into the bulk crystalline phase of porous NiO nanocubes (0.5 wt% Pt/NiO) can greatly promote the active phase (NiOOH) evolution. The Pt doping was achieved by a scalable nanocasting approach using SiO_2 as the hard template. In comparison with Pt/NiO samples with PtO_2 nanoparticles segregated at the NiO surface (1 wt% Pt), as well as atomistic Pt atoms solely bound at the surface by atomic layer deposition, the bulk Pt doping shows the strongest power in facilitating active phase transformation, which leads to improved OER activity with reduced overpotential and Tafel slope. Experiential data revealed that the charge-transfer from Pt to Ni through O leads to a local weaker Ni–O bond. First principles calculations confirmed that rather than acting as an active site for the OER, monatomic Pt effectively increases the phase transformation rate by reducing the migration barrier of nearby Ni atoms. Our discoveries reveal the relationships of the heteroatom doped structure and phase transformation behavior during the electrochemical process and offer a new route for designing high-performance electrocatalysts.

1. Introduction

Water electrolysis as the leading field of electrocatalysis is of significance for renewable energy development.[1–4] Noble metal single atom electrocatalysts (SAECs) have recently attracted great interest due to their intriguing physiochemical properties and unprecedented catalytic efficiency,[5–8] and facilitate a new strategy to synthesize efficient oxygen evolution reaction (OER) catalysts.[9–14] For instance, Au and Ir single atoms are found to be able to remarkably enhance the electrocatalytic activity of transition metal oxides and hydroxides.[13,14] Further research studies suggest that noble metal single atoms serve as the active sites, while some work indicates that 3d metals of supports with a tuned electronic state remained as active sites. Therefore, in SAECs, both noble metals and 3d metals may act as active sites, which however makes it challenging to distinguish their activity contribution. On the other hand, the surface layers of heterogeneous electrocatalysts especially under anodic oxidation potentials undergo pronounced phase transformation.[15] This phenomenon can be frequently observed even by the naked eye as the surface colour of bulk materials (*e.g.* metals, metal oxides and other derivatives) upon applying potential.[16] The presence of noble single atoms may also influence the kinetics of phase transition. Therefore, the activity contribution of SAECs is highly complicated, which can come from different sites (*i.e.* noble metal single atoms or 3d metals) or the *in situ* phase transition. However, the understanding of the enhanced OER activity on SACs is still poor.

The phase transition of heterogeneous electrocatalysts as one of the key steps in electrochemical reactions has been extensively investigated.[17,18] Since the phase transition involves crystal-to-crystal restructuring (*e.g.* oxide/hydroxide to oxy-hydroxide), the process is sluggish and requires extra over-potential in many cases.[19–22] NiO is a typical example, and has

[a]CAS Key Laboratory of Low-Carbon Conversion Science and Engineering, Shanghai Advanced Research Institute, Chinese Academy of Sciences, Shanghai 201210, China. E-mail: lixp@sari.ac.cn

[b]Collaborative Innovation Center of Chemistry for Energy Material, Key Laboratory of Computational Physical Science (Ministry of Education), Shanghai Key Laboratory of Molecular Catalysis and Innovative Materials, Department of Chemistry, Fudan University, Shanghai 200433, China. E-mail: yefeil@fudan.edu.cn

[c]Shanghai Synchrotron Radiation Facility, Shanghai Institute of Applied Physics, Chinese Academy of Sciences, Shanghai 201204, China. E-mail: jiangzheng@sinap.ac.cn

† Electronic supplementary information (ESI) available. See DOI: 10.1039/c8sc02015a

‡ Present address: Department of Materials and Chemical Engineering, Hanyang University, Ansan, Kyunggido 15588, Republic of Korea.

been widely studied due to its excellent resistance to corrosion in alkaline electrolysis.[23] However, the active phase transformation seems rather sluggish, and long-time ageing or constant cycling is required to 'preactivate' NiO.[24,25] Recent theoretical and experimental studies provide the insight that the electrocatalytic OER at NiO is not only limited to the surface, but also occurs in the bulk phase, because the transformed γ-NiOOH possesses a layered double hydroxide structure with a large intersheet space permitting the movement of hydroxide groups.[26,27] Such phase transition is highly favourable for OER activity enhancement. However, we noticed that there is very limited knowledge to promote such phase transition.

To address the aforementioned issues, herein, we intentionally doped poorly OER active Pt (0.5 wt%) into the bulk crystalline lattice of NiO. We demonstrated for the first time that Pt doping not only relies on introducing the secondary active site, but also accelerates the solid phase transformation from rocksalt NiO to active layered NiOOH during the OER. The enhanced active phase transformation of NiO led to a dramatic increase of electrochemical mass activity (MA). The MA of 0.5 wt% Pt/NiO is 3 orders of magnitude higher than that of NiO. More interestingly, the 0.5 wt% Pt/NiO exhibited 1.5-fold higher MA than 1 wt% Pt/NiO with PtO_2 nanoparticles segregated at the NiO surface and ALD-Pt/NiO with atomistic Pt atoms deposited at the surface (ALD denotes atomic layer deposition). This difference suggested that bulk doping is crucial to destabilizing the Ni–O bonds strongly held in the lattice. First principles calculations confirm that Pt single atoms do not serve as the active site, and this enhanced activity is due to the fact that monatomic Pt can promote the phase transition of NiO to γ-NiOOH, where the phase transition barrier is significantly reduced by 0.26 eV per f.u.

Our results are essential to understanding the activity enhancement of single atom electrocatalysts that involves phase transformation. Of note, deposition of noble metal nanoparticles (NP) has been frequently applied to boost the electrocatalytic activity of metal oxides (e.g. $AuNP/MnO_2$, Pt/CoO, $Au@FeO_x$, and Pd/CeO_2) by taking advantage of the strong electronic metal–support interaction.[28–31] However, common preparation methods such as impregnation, co-precipitation and sputtering may also lead to unintentional doping of single atoms that were hardly detectable by conventional characterization methods.[32–34] Our study may also contribute to understanding the origin of activity improvement of classic noble metal NP/oxide (or hydroxide, selenide, phosphide) electrocatalyst systems.

2. Results and discussion

2.1 Synthesis and characterization of Pt doped NiO nanocubes

Fig. 1a shows the schematic diagram of the nanocasting preparation process using SiO_2 as a template (Fig. S1 and S2†).[35,36] Bulk Pt doped NiO nanocubes were obtained by impregnation, drying and calcination in air, and template removal via NaOH etching, and the nominal Pt loading amount was 0.5 wt%. Such an impregnation & calcination process can be consistently and

cost-effectively up-scaled. Preparation of a single batch of over 200 g porous 0.5 wt% Pt/NiO nanocubes was demonstrated using this nanocasting approach (see the photograph in Fig. 1a). A control Pt/NiO sample with 1 wt% Pt nominal loading was also prepared using the same protocol. Besides, NiO with Pt atoms solely bound to the surface (denoted as ALD-Pt/NiO), which was prepared using an atomic layer deposition method, was also prepared for the purpose of comparison. Fig. S3† shows the thermogravimetric analysis (TGA) curve of porous silica, co-impregnated with $Ni(NO_3)_2$ and $Pt(NO_3)_2$ after drying, suggesting that metal nitrate precursors can be fully converted into the oxide phase upon calcination at 500 °C for 2 h. The X-ray diffraction (XRD) pattern (Fig. 1b) of 0.5 wt% Pt/NiO can be assigned to face centered cubic NiO crystals (JCPDS no. 47-1049).[37,38] No platinum oxide related phase was observed in 0.5 wt% Pt/NiO, indicative of high Pt dispersion.

Scanning electron microscopy (SEM) characterization revealed that 0.5 wt% Pt/NiO shared identical porous nanocube morphology with pure NiO (Fig. 1c and S4†). The nanocube size is in the range from 50 to 150 nm. The textural properties of the 0.5 wt% Pt/NiO nanocubes were elucidated by N_2 adsorption–desorption isotherms and pore size distribution. As displayed in Fig. S5,† 0.5 wt% Pt/NiO nanocubes possess an H1 type loop line with a surface area of 74.4 m^2 g^{-1} and a bimodal pore size distribution around 6.9 and 52.2 nm.[39] TEM characterization gives more microstructure details (Fig. 1d). The void size in the nanocubes was found to be in the range of 5–10 nm, suggesting a precise positive replication of the parent template. Such a hierarchical nature of the microstructure has been proved to be an ideal structure for application in the areas of catalysis and electrochemistry.[40–43] The existence of homogeneously distributed Pt was confirmed by energy dispersive spectroscopy (EDS) elemental mapping (Fig. S6†). Aberration-corrected high angle annular dark field-scanning transmission electron microscopy (HAADF-STEM) with sub-angstrom resolution was carried out to further investigate the dispersion state of Pt in the nanocubes, since it is capable of visualizing sub-nanometer metal particles or atoms of high atomic number (Z) with an unambiguous contrast. Fig. 1e shows the high resolution HAADF-STEM image of 0.5 wt% Pt/NiO; the Pt atom appears much brighter than the surrounding Ni atoms, while the lighter oxygen atoms are not detected. The line profiles of the HAADF signal, drawn from Fig. 1e, are displayed in Fig. 1f; the Pt and Ni atoms are clearly discernible. The Pt–Ni interatomic distance is estimated to be 1.82 Å, and the Ni–Ni spacing is estimated to be 1.46 Å, which generally agrees with the interplanar spacing of the NiO (220) plane (1.48 Å). These observations indicate that Pt was effectively substituted into the crystal lattice, occupying the Ni sites. In contrast, we find that once the nominal Pt loading amount exceeded 1 wt%, platinum easily nucleated on the surface of NiO nanocubes. Tiny Pt based particles with less than 2 nm diameter can be spotted in Fig. S7,† exhibiting a brighter contrast. The ALD-Pt/NiO was also characterized. The HAADF-STEM image reveals no existence of bright Pt nanoparticles and the corresponding EDS elemental mapping of atoms shows Pt atoms conformably coated on the surface of NiO nanocubes. The Pt loading amount was determined to be 0.42 wt% (Fig. S8†).
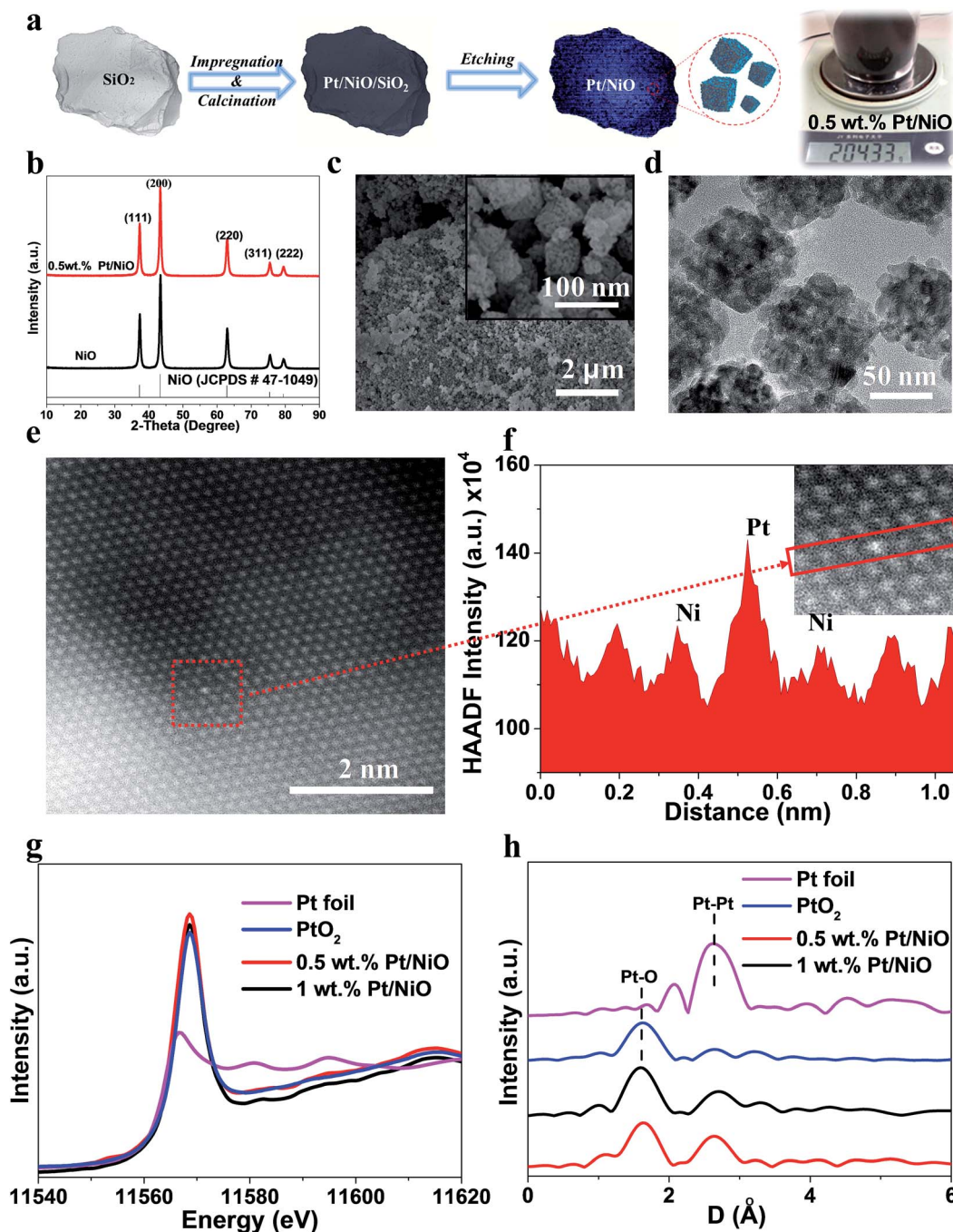
Fig. 1 (a) Schematic diagram of the preparation procedure of bulk single-atom Pt doped NiO nanocubes; the inset photograph shows a batch preparation of 200 g 0.5 wt% Pt/NiO nanocubes. (b) XRD patterns of pure porous NiO (black) and 0.5 wt% Pt/NiO nanocubes (red). (c) SEM image of porous 0.5 wt% Pt/NiO nanocubes; the inset is a magnified view of 0.5 wt% Pt/NiO nanocubes. (d) TEM image and (e) high resolution HAADF-STEM image of 0.5 wt% Pt/NiO. (f) HAADF signal analysis of 0.5 wt% Pt/NiO; the red square and arrow indicate the analyzed region. (g) The normalized XANES spectra at the Pt L3 edge and (h) the $k3$-weighted Fourier transform spectra from EXAFS spectra of the 0.5 wt% and 1 wt% Pt/NiO samples, and PtO_2 and Pt foil references.

While the HAADF-STEM characterization directly gave local crystal information, X-ray absorption spectroscopy (XAS) measurements were conducted to collectively investigate the geometric and electronic structures in ensembles of Pt in the samples. Fig. 1g shows the normalized X-ray absorption near-edge structure (XANES) spectra of samples of 0.5 wt% Pt/NiO and 1 wt% Pt/NiO, and the reference samples of Pt foil and PtO_2. A comparison between the references, bulk PtO_2 and Pt foil, provides evidence that the chemical states of Pt in both samples are similar to that of PtO_2 in terms of edge position and the intensity of the white line. The intensity of the white line reflects the vacancy population of the 5d orbital of Pt, whereas

the position of the white line reflects the energy difference between the initial state and the final state of the excited electrons. From Fig. 1g, we observed that the subtle difference in intensity of the white line, and hence the degree of 5d orbital vacancy, follows the order of PtO_2 < 1 wt% Pt/NiO < 0.5 wt% Pt/NiO. Apparently, the fact that the intensity of the white line in 0.5 wt% Pt/NiO is higher than that in 1 wt% Pt/NiO can be attributed to the stronger interaction between atomically dispersed Pt and NiO, indicative of a relatively higher binding energy of Pt in the 0.5 wt% Pt/NiO sample. It is also reported that, in a Pt_1/FeO_x system, there is an increase in the oxidation state of Pt. This means that the single atom Pt over the oxide will also induce charge transfer between metal atoms and the host oxide, reflecting a strong electronic metal–support interaction.[44–46]

To further verify the atomic dispersion of Pt throughout the 0.5 wt% Pt/NiO sample, Fourier transforms (FTs) of k^3-weighted extended X-ray absorption fine structure (EXAFS) oscillations at the Pt L3-edge were obtained for the samples as well as the references (Fig. 1h).[47,48] Consistent with the XANES analysis, the FTs of the EXAFS spectra of the samples revealed the oxidation states. The first prominent peak (without phase correction) at around ~1.7 Å corresponds to the Pt–O contribution, and the second peak at around ~2.8 Å is attributed to the Pt–Pt or Pt–Ni contribution. In order to further resolve the contributing factors for the second peak, we carried out EXAFS curve-fitting (the fitting parameters are given in Table S1†). From the above EXAFS analysis, the oxidation state of Pt in both samples was found to be +4. Hence, we set the coordination number of Pt–O at 6.0 in accordance with the structure of the reference PtO_2 sample. From Fig. 1h, we observed that the Pt–O bond length is close to that in PtO_2 with the corresponding values of 2.00 Å for the 0.5 wt% Pt/NiO, and 2.01 Å for the 1 wt% Pt/NiO sample. According to the results of HAADF-STEM, the Pt–O coordination most probably originated from the interaction between Pt and the NiO support. For the 0.5 wt% Pt/NiO sample, there is a Pt–Ni contribution observed at a distance of 3.00 Å, reflecting an average coordination number of 5.5. As the nearest neighbours of Pt are O atoms, the Pt–Ni coordination originates from the second-shell coordinator Ni, bridged by the O atoms. The EXAFS data did not reveal any Pt–Pt contribution in 0.5 wt% Pt/NiO, which can be confirmed by the comparison of three different fitting models (Fig. S9 and Table S2†). The above characterizations, including XRD, HAADF-STEM and EXAFS, provide solid evidence that single atom dispersion of Pt was realized in 0.5 wt% Pt/NiO.

2.2 Electrocatalytic performance and characterization of Pt/NiO

The OER performance of the as-prepared porous nanocubes, including NiO, 0.5 wt% Pt/NiO, 1 wt% Pt/NiO and ALD-Pt/NiO, was evaluated using cyclic voltammetry (CV) in 1 M rigorously Fe-free KOH solution at room temperature (Fig. 2a and S10†).[49] Fig. 2a shows the iR-corrected CV curves of 0.5 wt% Pt/NiO recorded for 500 cycles, which exhibited typical oxidation and reduction peaks, resulting from the oxidation of hydrated NiO

(i.e. $Ni(OH)_2$) to NiOOH, and its reduction to $Ni(OH)_2$ in each CV cycle.[50] The redox peak progressively shifted anodically with increasing CV cycles, forming a step of 2–4 mV per 100 cycles. Meanwhile, the current density at 1.6 V increased by more than 2 orders of magnitude after 100 cycles, and almost 3 orders of magnitude after 200 cycles, and finally, the CV stabilized after 200 cycles. All the control samples exhibited a similar progressive change of CVs. However, each sample required a different number of cycles to reach stabilization, and showed a different OER performance enhancement after cycling. ALD-Pt/NiO and 1 wt% Pt/NiO took 100 and 200 cycles, respectively, and pure NiO required 400 cycles for reaching stabilization. Fig. 2b shows the iR-corrected CV curves of all the samples after 500 electrochemical cycles. The OER activity generally followed the order 0.5 wt% Pt/NiO > ALD-Pt/NiO > 1 wt% Pt/NiO > NiO. The overpotentials required by 0.5 wt% Pt/NiO to achieve 10 and 50 mA cm^{-2} were 358 mV and 400 mV, respectively, while NiO required an overpotential of 510 mV to deliver 10 mA cm^{-2}. We also found that other PGM metals such as Rh also remarkably enhanced the OER performance of NiO (Fig. S11†) as Pt did. To ensure that the OER performance enhancements were not caused by Fe contamination, we carried out inductively coupled plasma optical emission spectrometry (ICP-OES) measurements of the used electrolyte. No Fe was detected. Interestingly, we detected a trace amount of Pt ions (0.548 ppm), which were partially leached into the electrolyte due to restructuring of NiO. To highlight the advantage of Pt doping, we intentionally doped NiO with 0.5 wt% Fe. The 0.5 wt% Fe/NiO showed inferior OER performance as compared to 0.5 wt% Pt/NiO (Fig. S12†). The catalyst mass activity (MA) of 0.5 wt% Pt/NiO was as high as 508 A g^{-1} at an overpotential of 400 mV, whereas the mass activity of 1 wt% Pt/NiO and ALD-Pt/NiO ranged from 19 to 331 A g^{-1} at the same overpotential (Fig. 2d).[51] The Pt doping not only enabled a substantial increase of the OER activity, but also improved the OER kinetics as reflected by Tafel analysis (Fig. 2c) The Tafel slope of 0.5 wt% Pt/NiO after 500 cycles was only 33 mV dec^{-1}, which was the smallest among all cycled samples. Electrochemical impedance spectroscopy (EIS) was conducted to gain insight into the reaction kinetics (Fig. S13†). The Nyquist plot showed that bulk Pt doping markedly reduced the charge transfer resistance (R_{ct}) of NiO from 19.85 Ω to 4.80 Ω. Of note, when the mass loading of Pt was further increased to 1 wt% Pt, the R_{ct} increased to 5.4 Ω due to segregation of Pt at the NiO surface. These results confirmed the positive effect of Pt single atoms on promoting OER kinetics.

2.3 Probing and understanding the active phase transformation powered by Pt single atoms

Based on the above CV results, the promotional effect on the OER performance by single-atom Pt doping (0.5 wt%) into the body of NiO is most significant among all Pt/NiO samples. High resolution X-ray photoelectron spectroscopy (XPS) measurements were carried out, specifically to investigate the chemical changes before and after the continuous CV cycling. Fig. 3a–d show the photoemission envelope of Ni $2p_{3/2}$ before electrochemical cycling. The experimental spectra have been fitted to
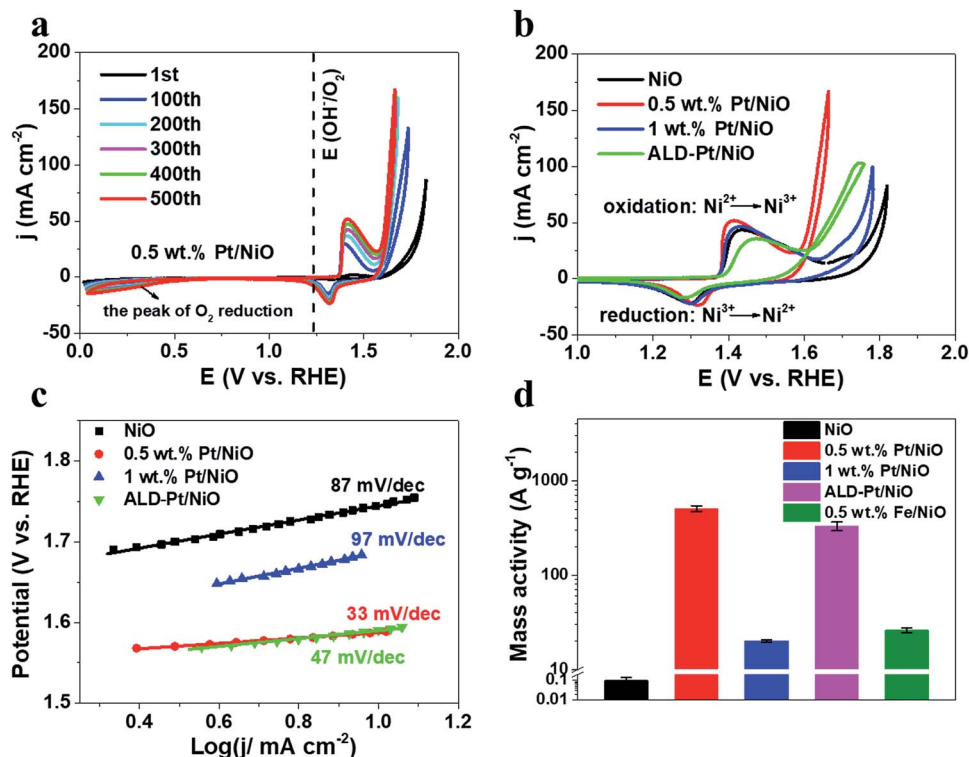
Fig. 2 (a) CV curves at the 1st, 100th, 200th, 300th, 400th and 500th cycles for the 0.5 wt% Pt/NiO catalyst, recorded at a sweep rate of 100 mV s^{-1}. (b) Comparison of the CV curves of pure NiO, 0.5 wt% Pt/NiO, 1 wt% Pt/NiO and ALD-Pt/NiO catalysts. All CV curves were recorded at a sweep rate of 10 mV s^{-1} after 500 cycles. (c) Tafel plots of all Pt/NiO samples after 500 electrochemical cycles were derived from (b) using the cathode sweep to avoid interference from the oxidation peak. (d) Mass activity of pure NiO, 0.5 wt% Pt/NiO, 1 wt% Pt/NiO and ALD-Pt/NiO catalysts at an overpotential of 400 mV. All of the CV curves were iR-compensated. The catalyst loading was set as 0.1 mg cm^{-2}.

a set of six peaks with a Gaussian/Lorentzian ratio of 0.7 (i.e. 70% Gaussian shape contribution), denoted from A to F for simplicity. The components appearing at 853.7 eV (A), 860.7 eV (D) and 863.5 eV (E) are assigned to the $\underline{c}d^9\underline{L}$, $\underline{c}d^{10}\underline{L}^2$, and $\underline{c}d^8$ states, respectively (i.e. $\underline{c}$ represents a hole in the 2p level and $\underline{L}$ denotes a hole in a ligand orbital),[23,52] originating from an on-site charge-transfer (CT) process between ligand anions and the Ni cation. The components at 855.4 eV (B) and 856.7 eV (C) are attributed to an inter-site CT screening process, whereas component F is attributed to shake-up transitions.[23] According to previous literature, peak A can be as associated with Ni(II) species, while the intensity of peaks B and C can reflect the amount of Ni with higher valence (i.e. Ni(III)).[23,53] As shown in Fig. 3e–h, it is evident that peak A vanished after the electrochemical cycling for all of the catalysts. This suggested that Ni(II)O was transformed into Ni(III)OOH within the detection depth of XPS (<2 nm), which has been identified as the key active phase catalyzing the OER by previous in situ Raman, XPS and XAS studies;[23,54,55] this is also in line with the CV results. The structural change of 0.5 wt% Pt/NiO with repeated cycling was also analyzed ex situ by TEM (Fig. S14†). No pulverization of the electrocatalysts was observed. The nanocubes retained their crystalline phase and still preserved their porous geometry after 500 cycles. The HRTEM image revealed clear lattice fringes with an interlayer spacing of 0.237 nm, corresponding to the (102) plane of γ-NiOOH.[56,57] We believe that Pt incorporation can

enrich the Ni(III) species in NiO nanocubes and subsequently facilitate the formation of an active γ-NiOOH phase, which is close to the scenario of Co incorporation into Ni–Co oxide hierarchical nanosheets.[52] As previously inferred from the XANES study, higher binding energy of Pt appears in the 0.5 wt% Pt/NiO sample as compared to that for 1 wt% Pt/NiO, implying charge-transfer from Pt to Ni through O. This would lead to a locally weaker Ni–O bond, and consequently promote the formation of catalytically active NiOOH sites on the surface of NiO nanocubes.[55]

It is worth noting that ALD-Pt/NiO had faster OER current stabilization (100 cycles) than 0.5 wt% Pt/NiO (200 cycles) and NiO (400 cycles), indicating its faster phase transformation (Fig. 3i). In comparison with 0.5 wt% Pt/NiO with a majority of Pt atoms embedded in the bulk, atomic Pt species in ALD-Pt/NiO were exclusively exposed at the NiO surface. This difference leads us to consider that bulk Pt doping has an obvious advantage in accelerating the active phase evolution during the OER. To compare the extent of phase transition for NiO, 0.5 wt% Pt/NiO and ALD-Pt/NiO, XPS depth profile analysis was carried out (Fig. 3j–l). The atomic ratios of Ni/O at the surface of all the samples are in accord with the stoichiometric number of NiOOH, but gradually approach that of NiO with the increase of depth. The thickness of the NiOOH phase was estimated to follow the order 0.5 wt% Pt/NiO > ALD-Pt/NiO > NiO, agreeing with the activity order. The results draw us to conclude that Pt
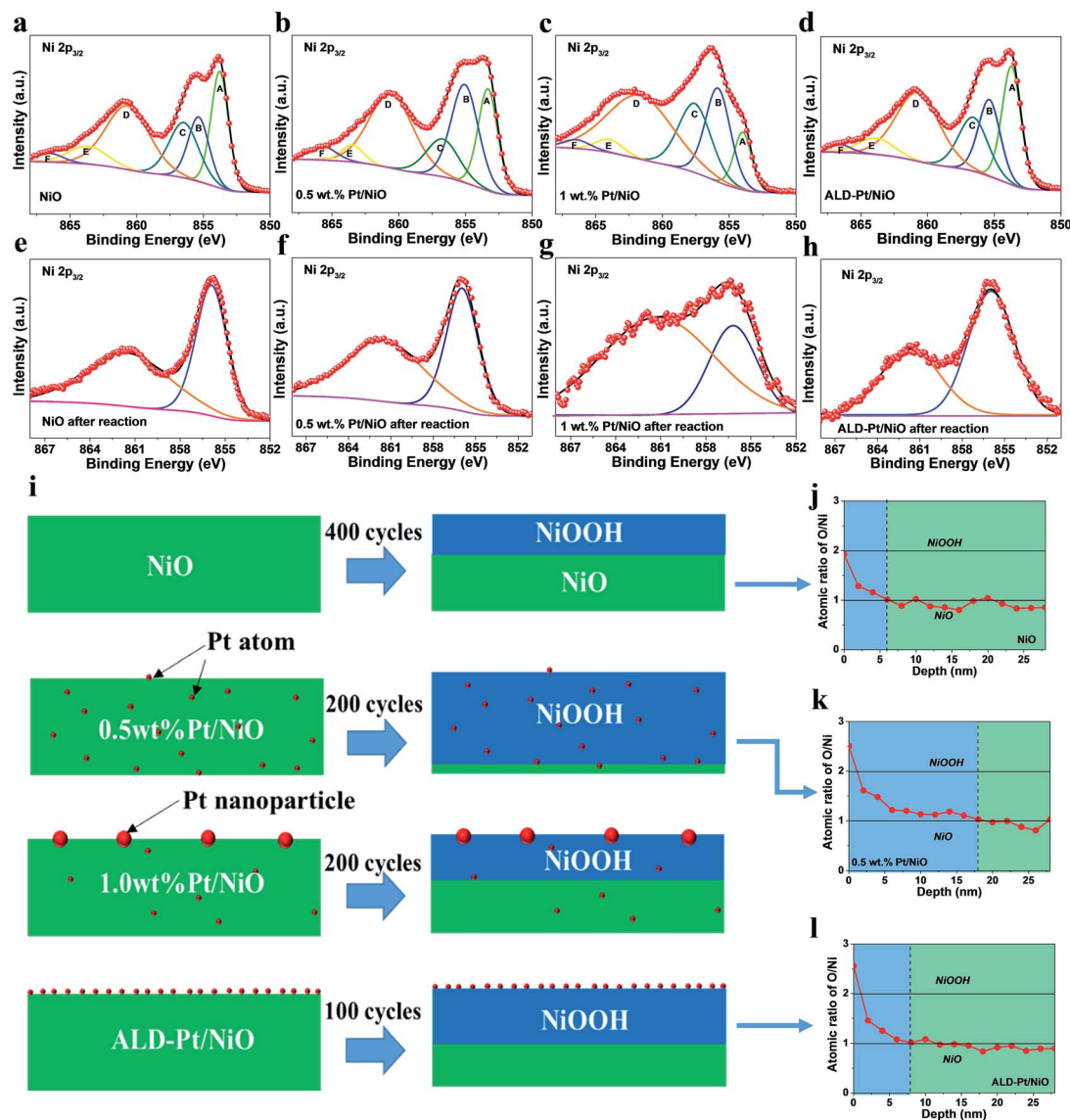
Fig. 3 Ni $2p_{3/2}$ spectra of the as-prepared (a) NiO, (b) 0.5 wt% Pt/NiO, (c) 1 wt% Pt/NiO and (d) ALD-Pt/NiO and (e−h) the corresponding Ni $2p_{3/2}$ spectra obtained after 500 electrochemical cycles. (i) Schematic diagrams of the phase transformation behavior for all of the catalysts and the minimum cycle number required to complete phase transition for the corresponding sample. XPS depth profiles for (j) pure NiO, (k) 0.5 wt% Pt/NiO, and (l) ALD-Pt/NiO after 500 electrochemical cycles.

single atoms can promote the NiO to NiOOH phase transformation that is beneficial for OER activity improvement. And the phase transformation can proceed from the surface to the bulk; therefore bulk Pt doping can facilitate a more pronounced in-depth phase transformation than surface deposition of Pt.

To clarify the origin of the enhanced OER activity for Pt/NiO, we performed first principles calculations to gain insights into the active sites and phase transformation behaviour. First, we investigated the intrinsic activity of the OER on the active γ-NiOOH phase.[50,58,59] To this end, we calculated the theoretical overpotential on both Ni and Pt sites using a computational hydrogen electrode (CHE) model. In this calculation approach, the proton and electron free energies are replaced by the H_2 molecule and electrode potential versus the Standard Hydrogen
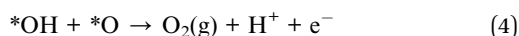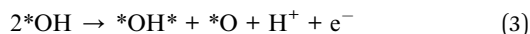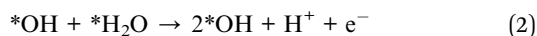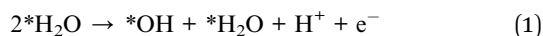
Electrode (SHE), while the details of the CHE model can be found in the ESI.†

It should be mentioned that the calculation of theoretical overpotential in the CHE approach is far from straightforward, where the definition of theoretical overpotential based on the thermodynamics does not directly correspond to the experimental overpotential, indicating that there may exist differences between them. Fortunately, Norskov et al. have pointed out that although quantitative comparison between theoretical and experimental overpotentials is difficult, the theoretical overpotential is consistent with the experimental overpotential, following a qualitative trend.[60] Therefore, in the following discussions, we should focus on the qualitative comparison between theoretical overpotentials of different materials, and

should not relate the theoretical overpotential with the experimental overpotential directly.
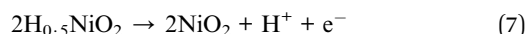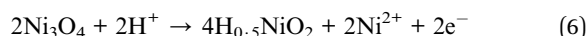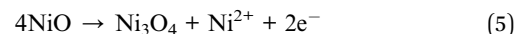
The key intermediates are shown in Fig. 4a, where the O atoms of two water molecules involved in the OER are marked with arrows. Calculations show that the OER proceeds *via* the following four-step mechanism.

$$2*H_2O \rightarrow *OH + *H_2O + H^+ + e^- \tag{1}$$

$$*OH + *H_2O \rightarrow 2*OH + H^+ + e^- \tag{2}$$

$$2*OH \rightarrow *OH* + *O + H^+ + e^- \tag{3}$$

$$*OH + *O \rightarrow O_2(g) + H^+ + e^- \tag{4}$$

In the formula, the asterisk (*) denotes the exposed Ni or Pt ion at the edge of γ-NiOOH. In steps i and ii, two protons of two water molecules are released sequentially into the aqueous solution, resulting in two adjacent *OH (2*OH, Fig. 4). Then in step iii, a proton of *OH is further released, and the remaining *O bond with lattice O to form O–O peroxo species (*OH + *O, Fig. 4). In step iv, the fourth proton is released and an O_2 molecule evolves from the surface. The energy profiles in Fig. 4b show that the theoretical overpotential is 200 mV for pure γ-NiOOH, while for the Pt dopant, it increases to 420 mV. Thus, the Pt dopant shows lower activity than Ni for the OER, and is not the active site for Pt/NiO.

Next, we investigated the influence of Pt dopant on the kinetics of phase transition, which may also have an impact on the kinetics of phase transformation besides the OER activity. One notable change of the phase transition is that the ratio of Ni : O changes from 1 : 1 in NiO to 1 : 2 in γ-NiOOH. This transformation is not a simple solid-to-solid phase transition, but also involves a variety of chemical compositions. Therefore, we need to first determine the chemical composition when the phase transition occurs before sampling the pathway of phase transition. Here, we investigate the phase transition *via* a two-step approach: (i) calculating the phase diagram to determine the chemical component when the solid-to-solid phase transition begins, and (ii) performing stochastic surface walking (SSW) pathway sampling to clarify the mechanism of phase transition. The algorithm of SSW pathway sampling was elaborated in our previous papers,[61–64] and includes basically two parts: (i) SSW sampling to identify all possible reaction coordinates, and (ii) a variable-cell double-ended surface walking (VC-DESW) method to locate the transition state (TS) in the low energy reaction pathway (see also the ESI† for the methodology). This approach was recently utilized to investigate the mechanism of a series of phase transitions on ZrO_2,[65] TiO_2,[66] MnO_2 (ref. 67) and graphite.[68] To determine the nascent chemical component of NiO_x, we plotted the phase diagram of four selected components, namely NiO, Ni_3O_4, $H_{0.5}NiO_2$, and NiO_2. It should be mentioned that during the phase transition, half of the Ni ions in NiO dissolved in the electrolyte. By randomly removing half of the lattice Ni ions from NiO, we can immediately find that the remaining structure is a spinel-like structure (Fig. S15†). As a result, herein we focus on the spinel form of Ni_3O_4, $H_{0.5}NiO_2$, and NiO_2. The transformations between these phases follow eqn (5)–(7).

$$4NiO \rightarrow Ni_3O_4 + Ni^{2+} + 2e^- \tag{5}$$

$$2Ni_3O_4 + 2H^+ \rightarrow 4H_{0.5}NiO_2 + 2Ni^{2+} + 2e^- \tag{6}$$

$$2H_{0.5}NiO_2 \rightarrow 2NiO_2 + H^+ + e^- \tag{7}$$

The calculated phase diagram is shown in Fig. 5, where NiO is set as the reference phase (the horizontal line). The calculation details can also be found in the ESI.† Since the initial NiO phase is taken as the reference, its free energy is set as zero (the horizontal line in the phase diagram). The calculation details of the phase diagram can be found in the ESI.† Our results show that $H_{0.5}NiO_2$ is the stable phase under OER conditions ($\sim$1.23 V). Thus, we used spinel $H_{0.5}NiO_2$ as the initial state to perform SSW pathway sampling to investigate the kinetics of phase transition.
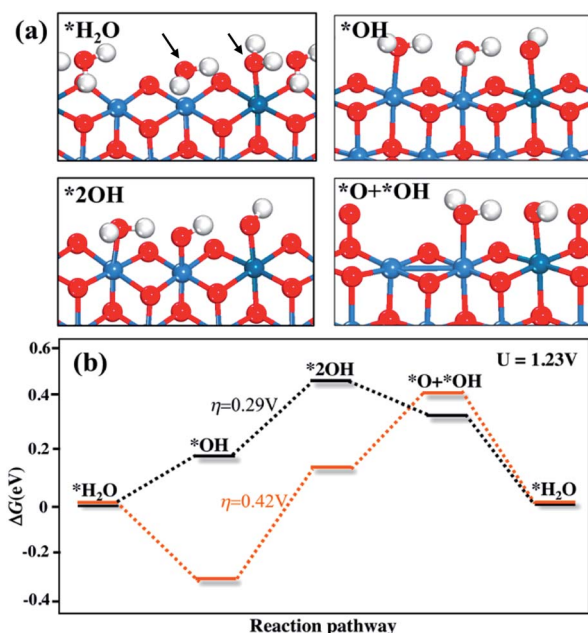

Fig. 4 (a) Simulated OER element steps proceeded at the Pt doped γ-NiOOH. White, red, blue and dark cyan balls represent H, O, Ni and Pt, respectively. (b) The energy profiles of the OER at potential $U = 1.23$ V.
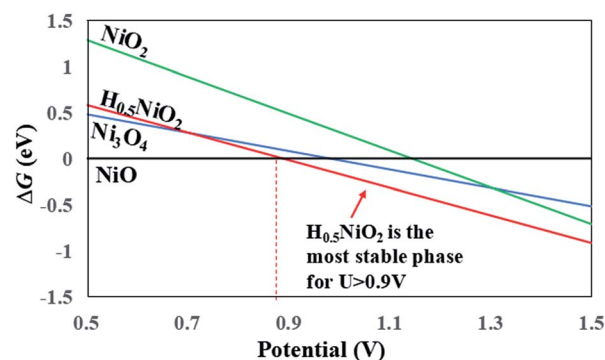

Fig. 5 Calculated phase diagram for NiO, Ni_3O_4, $H_{0.5}NiO_2$ and NiO_2.

Starting from the spinel $H_{0.5}NiO_2$ phase, we performed SSW pathway sampling to calculate the lowest energy pathway for the formation of γ-NiOOH. The details for phase transition calculations can be found in the ESI.† We first investigated the energy profiles of phase transition on pure NiO, and the key intermediate structures are shown in Fig. 6. The lowest energy pathway of the spinel-to-layer transition contains three steps, as shown in Fig. 6b. In the first step, spinel → TS1 → MS1, intercalated Ni (Ni^{ic}, as indicated by an arrow in the spinel phase of Fig. 6a) migrates from the A to the B hollow site of the bottom NiO_2 layer, accompanied by a shearing movement of NiO_2 layers along [1$\bar{2}$10]. This step has a barrier of 0.34 eV per fu. At the transition state (TS), i.e. TS1, Ni^{ic} locates at the lattice O bridge site between A and B sites, leading to a decrease of the coordination number (CN) of Ni^{ic} from 6 in the spinel phase to 5 in TS1. In the subsequent step, MS1 → TS2 → MS2, Ni^{ic} further migrates by ~2.5 Å assisted by a shearing movement of NiO_2 layers along [11$\bar{2}$0] by ~1/2 lattice. At the end of this step, Ni^{ic} occupies an interlayer position right above a Ni vacancy in the B site of the bottom NiO_2 layer. This step is kinetically facile with a low transition barrier (MS1 → TS2) of 0.10 eV per fu. In the final step, MS2 → TS3 → γ-NiOOH, Ni^{ic} sinks into the Ni vacancy of the bottom NiO_2 layer, resulting in γ-NiOOH. In TS3, Ni^{ic} locates in the O plane of the NiO_2 layer, where all bonds of Ni^{ic} with the top NiO_2 layer break at this state. This significant structural change causes a large overall barrier (spinel → TS3) of 0.43 eV per fu, and this step is the rate-determining step in the phase transition.

Next, we investigated the kinetics of phase transition on Pt/NiO, where one Ni ion in the unit cell is replaced by a Pt dopant. The phase transition may occur via the two following pathways: (i) the Pt dopant migrates within the NiO lattice and sinks into the Ni vacancy of the NiO_2 layer; (ii) Ni migrates within the NiO lattice and sinks into the Ni vacancy near the Pt dopant. For the first pathway, our calculations show that the overall transition barrier is 0.7 eV per fu, significantly higher than that of pure NiO (0.43 eV per fu), indicating that it is difficult for the Pt dopant to diffuse within the NiO lattice. As for the second pathway, we found that the overall barrier reduces to 0.17 eV per fu (see Fig. 6b), lower than that of pure NiO. Therefore, we conclude that the monatomic Pt doping can significantly increase the rate of phase transition. A movie showing the dynamic phase transformation of Pt doped NiO is provided in the ESI.†

3. Conclusions

In summary, for the first time, we discovered that Pt, previously regarded as a lousy OER electrocatalyst, in its single atom form has unique power in enhancing and accelerating OER active NiOOH phase transformation from NiO in alkaline media. Bulk Pt doping (0.5 wt% Pt/NiO) was identified as being advantageous over conventional atomistic doping with Pt atoms solely bound at the surface by facilitating a more pronounced in-depth bulk phase transformation. As a result, 0.5 wt% Pt/NiO possessed a remarkable mass activity of 508 A g^{-1} at an overpotential of 400 mV, and outperformed NiO, ALD-Pt/NiO, and 1 wt% Pt/NiO. First principles calculations show that the Pt dopant actually does not lower the overpotential of the OER. Instead, the presence of the Pt dopant weakens the nearby Ni–O bonds, leading to the activation of phase transition from NiO to γ-NiOOH, which is evident from the experimental finding that the surface of 0.5 wt% Pt/NiO is covered by thicker γ-NiOOH compared with that of pure NiO. Considering that phase transformation widely occurs in electrocatalytic reactions of metal oxides and non-metal oxides, our study provides a new perspective to design efficient electrocatalysts.

Conflicts of interest

There are no conflicts to declare.

Acknowledgements

Notes and references

1 A. Grimaud, O. Diaz-Morales, B. Han, W. T. Hong, Y.-L. Lee, L. Giordano, K. A. Stoerzinger, M. T. M. Koper and Y. Shao-Horn, Nat. Chem., 2017, 9, 457.

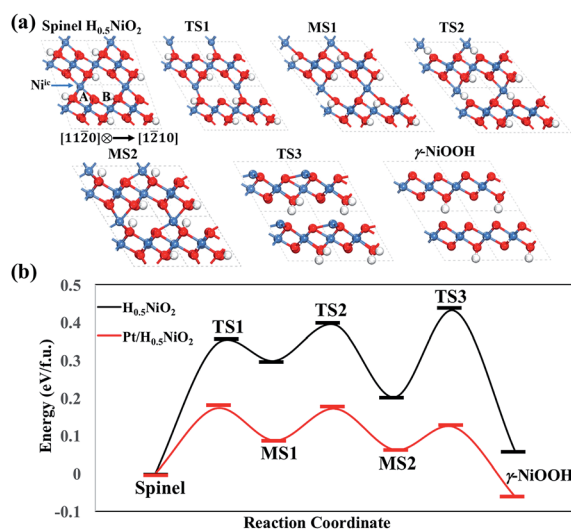2 L. Chen, X. Dong, Y. Wang and Y. Xia, Nat. Commun., 2016, 7, 11741.

Fig. 6 (a) Key intermediate structures for the reaction pathway of pure $H_{0.5}NiO_2$, and (b) energy profiles for phase transition from spinel $H_{0.5}NiO_2$ to γ-NiOOH for pure and Pt-doped $H_{0.5}NiO_2$.

3 O. Diaz-Morales, I. Ledezma-Yanez, M. T. M. Koper and F. Calle-Vallejo, *ACS Catal.*, 2015, **5**, 5380–5387.

4 Q. Zhao, Z. Yan, C. Chen and J. Chen, *Chem. Rev.*, 2017, **117**, 10121–10211.

5 X.-F. Yang, A. Wang, B. Qiao, J. Li, J. Liu and T. Zhang, *Acc. Chem. Res.*, 2013, **46**, 1740–1748.

6 Y. Chen, S. Ji, Y. Wang, J. Dong, W. Chen, Z. Li, R. Shen, L. Zheng, Z. Zhuang, D. Wang and Y. Li, *Angew. Chem., Int. Ed.*, 2017, **56**, 6937–6941.

7 C. Zhu, S. Fu, Q. Shi, D. Du and Y. Lin, *Angew. Chem., Int. Ed.*, 2017, **56**, 13944.

8 W. Liu, L. Zhang, W. Yan, X. Liu, X. Yang, S. Miao, W. Wang, A. Wang and T. Zhang, *Chem. Sci.*, 2016, **7**, 5758–5764.

9 J. Zhang, J. Liu, L. Xi, Y. Yu, N. Chen, S. Sun, W. Wang, K. M. Lange and B. Zhang, *J. Am. Chem. Soc.*, 2018, **140**, 3876–3879.

10 X. Li, P. Cui, W. Zhong, J. Li, X. Wang, Z. Wang and J. Jiang, *Chem. Commun.*, 2016, **52**, 13233–13236.

11 L. Liu and A. Corma, *Chem. Rev.*, 2018, **118**, 4981–5079.

12 C. Zhu, S. Fu, Q. Shi, D. Du and Y. Lin, *Angew. Chem., Int. Ed.*, 2017, **56**, 13944–13960.

13 X. Zhao, P. Gao, Y. Yan, X. Li, Y. Xing, H. Li, Z. Peng, J. Yang and J. Zeng, *J. Mater. Chem. A*, 2017, **5**, 20202–20207.

14 Y. Zhang, C. Wu, H. Jiang, Y. Lin, H. Liu, Q. He, S. Chen, T. Duan and L. Song, *Adv. Mater.*, 2018, **30**, 1707522.

15 S. Jin, *ACS Energy Lett.*, 2017, **2**, 1937–1938.

16 G. Ou, P. Fan, H. Zhang, K. Huang, C. Yang, W. Yu, H. Wei, M. Zhong, H. Wu and Y. Li, *Nano Energy*, 2017, **35**, 207–214.

17 H. Li, S. Chen, X. Jia, B. Xu, H. Lin, H. Yang, L. Song and X. Wang, *Nat. Commun.*, 2017, **8**, 15377.

18 C. Pengzuo, X. Kun, T. Shi, Z. Tianpei, T. Yun, D. Hui, Z. Lidong, C. Wangsheng, W. Changzheng and X. Yi, *Adv. Mater.*, 2016, **28**, 7527–7532.

19 R. L. Doyle and M. E. G. Lyons, *ECS Trans.*, 2013, **45**, 3–19.

20 C. Bocca, A. Barbucci, M. Delucchi and G. Cerisola, *Int. J. Hydrogen Energy*, 1999, **24**, 21–26.

21 L. Trotochaud, J. K. Ranney, K. N. Williams and S. W. Boettcher, *J. Am. Chem. Soc.*, 2012, **134**, 17253–17261.

22 M. R. G. de Chialvo and A. C. Chialvo, *Electrochim. Acta*, 1990, **35**, 437–443.

23 A. G. Marrani, V. Novelli, S. Sheehan, D. P. Dowling and D. Dini, *ACS Appl. Mater. Interfaces*, 2014, **6**, 143–152.

24 I. J. Godwin and M. E. G. Lyons, *Electrochem. Commun.*, 2013, **32**, 39–42.

25 S. Klaus, Y. Cai, M. W. Louie, L. Trotochaud and A. T. Bell, *J. Phys. Chem. C*, 2015, **119**, 7243–7254.

26 A. D. Doyle, M. Bajdich and A. Vojvodic, *Catal. Lett.*, 2017, 1–7.

27 L.-A. Stern and X. Hu, *Faraday Discuss.*, 2014, **176**, 363–379.

28 H. Zhang, C. Lin, F. Du, Y. Zhao, P. Gao, H. Chen, Z. Jiao, X. Li, T. Zhao and Y. Sun, *ACS Sustainable Chem. Eng.*, 2015, **3**, 2049–2057.

29 C. Meng, T. Ling, T. Y. Ma, H. Wang, Z. Hu, Y. Zhou, J. Mao, X. W. Du, M. Jaroniec and S. Z. Qiao, *Adv. Mater.*, 2017, **29**, 1604607.

30 H. A. Miller, F. Vizza, M. Marelli, A. Zadick, L. Dubau, M. Chatenet, S. Geiger, S. Cherevko, H. Doan,

R. K. Pavlicek, S. Mukerjee and D. R. Dekel, *Nano Energy*, 2017, **33**, 293–305.

31 A. L. Strickler, M. a. Escudero-Escribano and T. F. Jaramillo, *Nano Lett.*, 2017, **17**, 6040–6046.

32 H. Wei, X. Liu, A. Wang, L. Zhang, B. Qiao, X. Yang, Y. Huang, S. Miao, J. Liu and T. Zhang, *Nat. Commun.*, 2014, **5**, 5634.

33 L.-W. Guo, P.-P. Du, X.-P. Fu, C. Ma, J. Zeng, R. Si, Y.-Y. Huang, C.-J. Jia, Y.-W. Zhang and C.-H. Yan, *Nat. Commun.*, 2016, **7**, 13481.

34 Y. Zhu, Z. An and J. He, *J. Catal.*, 2016, **341**, 44–54.

35 T. Grewe, X. Deng, C. Weidenthaler, F. Schüth and H. Tüysüz, *Chem. Mater.*, 2013, **25**, 4926–4935.

36 X. Ning, Y. Lu, H. Fu, H. Wan, Z. Xu and S. Zheng, *ACS Appl. Mater. Interfaces*, 2017, **9**, 19335–19344.

37 X. Sun, X. Hu, Y. Wang, R. Xiong, X. Li, J. Liu, H. Ji, X. Li, S. Cai and C. Zheng, *J. Phys. Chem. C*, 2015, **119**, 3228–3237.

38 D. Delgado, B. Solsona, A. Ykrelef, A. Rodríguez-Gómez, A. Caballero, E. Rodríguez-Aguado, E. Rodríguez-Castellón and J. M. López Nieto, *J. Phys. Chem. C*, 2017, **121**, 25132–25142.

39 Z.-Q. Li, W.-C. Chen, F.-L. Guo, L.-E. Mo, L.-H. Hu and S.-Y. Dai, *Sci. Rep.*, 2015, **5**, 14178.

40 Y. Ouyang, X. Xia, H. Ye, L. Wang, X. Jiao, W. Lei and Q. Hao, *ACS Appl. Mater. Interfaces*, 2018, **10**, 3549–3561.

41 G. Huang, S. Xu, S. Lu, L. Li and H. Sun, *ACS Appl. Mater. Interfaces*, 2014, **6**, 7236–7243.

42 M. Prabu, K. Ketpang and S. Shanmugam, *Nanoscale*, 2014, **6**, 3173–3181.

43 G. Jia, Y. Hu, Q. Qian, Y. Yao, S. Zhang, Z. Li and Z. Zou, *ACS Appl. Mater. Interfaces*, 2016, **8**, 14527–14534.

44 B. Qiao, A. Wang, X. Yang, L. F. Allard, Z. Jiang, Y. Cui, J. Liu, J. Li and T. Zhang, *Nat. Chem.*, 2011, **3**, 634–641.

45 S. Chauhan, T. Mori, T. Masuda, S. Ueda, G. J. Richards, J. P. Hill, K. Ariga, N. Isaka, G. Auchterlonie and J. Drennan, *ACS Appl. Mater. Interfaces*, 2016, **8**, 9059–9070.

46 T. Masuda, H. Fukumitsu, K. Fugane, H. Togasaki, D. Matsumura, K. Tamura, Y. Nishihata, H. Yoshikawa, K. Kobayashi, T. Mori and K. Uosaki, *J. Phys. Chem. C*, 2012, **116**, 10098–10102.

47 H. S. Yu, X. J. Wei, J. Zheng and Y. Y. Huang, *Nucl. Sci. Tech.*, 2015, **26**, 050102.

48 B. Ravel and M. Newville, *J. Synchrotron Radiat.*, 2005, **12**, 537–541.

49 F. Calle-Vallejo, M. T. M. Koper and A. S. Bandarenka, *Chem. Soc. Rev.*, 2013, **42**, 5210–5230.

50 M. Gao, W. Sheng, Z. Zhuang, Q. Fang, S. Gu, J. Jiang and Y. Yan, *J. Am. Chem. Soc.*, 2014, **136**, 7077–7084.

51 X. Xu, C. Su, W. Zhou, Y. Zhu, Y. Chen and Z. Shao, *Adv. Sci.*, 2016, **3**, 1500187.

52 B. S. Yeo and A. T. Bell, *J. Phys. Chem. C*, 2012, **116**, 8394–8400.

53 H.-Y. Wang, Y.-Y. Hsu, R. Chen, T.-S. Chan, H. M. Chen and B. Liu, *Adv. Energy Mater.*, 2015, **5**, 1500091.

54 O. Diaz-Morales, D. Ferrus-Suspedra and M. T. M. Koper, *Chem. Sci.*, 2016, **7**, 2639–2645.

55 J. D. Michael, E. L. Demeter, S. M. Illes, Q. Fan, J. R. Boes and J. R. Kitchin, *J. Phys. Chem. C*, 2015, **119**, 11475–11481.

56 A. Agrawal, H. R. Habibi, R. K. Agrawal, J. P. Cronin, D. M. Roberts, R. S. Caron-Popowich and C. M. Lampert, *Thin Solid Films*, 1992, **221**, 239–253.

57 M. Wang, M. Lin, J. Li, L. Huang, Z. Zhuang, C. Lin, L. Zhou and L. Mai, *Chem. Commun.*, 2017, **53**, 8372–8375.

58 D. K. Bediako, B. Lassalle-Kaiser, Y. Surendranath, J. Yano, V. K. Yachandra and D. G. Nocera, *J. Am. Chem. Soc.*, 2012, **134**, 6801–6809.

59 R. D. L. Smith and C. P. Berlinguette, *J. Am. Chem. Soc.*, 2016, **138**, 1561–1567.

60 I. C. Man, H.-Y. Su, F. Calle-Vallejo, H. A. Hansen, J. I. Martínez, N. G. Inoglu, J. Kitchin, T. F. Jaramillo, J. K. Nørskov and J. Rossmeisl, *ChemCatChem*, 2011, **3**, 1159–1165.

61 X.-J. Zhang and Z.-P. Liu, *J. Chem. Theory Comput.*, 2015, **11**, 4885–4894.

62 X.-J. Zhang, C. Shang and Z.-P. Liu, *J. Chem. Theory Comput.*, 2013, **9**, 5745–5753.

63 C. Shang, X.-J. Zhang and Z.-P. Liu, *Phys. Chem. Chem. Phys.*, 2014, **16**, 17845–17856.

64 C. Shang and Z.-P. Liu, *J. Chem. Theory Comput.*, 2013, **9**, 1838–1845.

65 S.-H. Guan, X.-J. Zhang and Z.-P. Liu, *J. Am. Chem. Soc.*, 2015, **137**, 8010–8013.

66 S.-C. Zhu, S.-H. Xie and Z.-P. Liu, *J. Am. Chem. Soc.*, 2015, **137**, 11532–11539.

67 Y.-F. Li, S.-C. Zhu and Z.-P. Liu, *J. Am. Chem. Soc.*, 2016, **138**, 5371–5379.

68 Y.-P. Xie, X.-J. Zhang and Z.-P. Liu, *J. Am. Chem. Soc.*, 2017, **139**, 2545–2548.